The International Journal of Advanced Manufacturing Technology
https://doi.org/10.1007/s00170-025-15854-8

ORIGINAL ARTICLE

Effects of machine compliance on forming accuracy and forces in SPIF of AISI 430

Alejandro Simoncelli[1,2] · Luciano Buglioni[1] · Daniel Martínez Krahmer[1] · Antonio Sánchez Egea[2]

Received: 11 April 2025 / Accepted: 31 May 2025

Abstract

Single Point Incremental Forming (SPIF) is a versatile process for producing small batches or custom components in precision-demanding industries. This dieless metal forming technique utilizes a hemispherical-tipped tool that follows a controlled trajectory. While SPIF offers flexibility and high formability, challenges related to geometric accuracy and springback persist. This study investigates the impact of machine compliance on geometric accuracy and forming forces during stainless steel SPIF using both a CNC machine and a robot, combining experimental tests and FEM analysis. The results reveal that the CNC machine is approximately 2.5×, 4×, and 11× stiffer than the robot in the X, Y, and Z directions, respectively. CNC-formed parts demonstrated lower wall angle deviations (e.g., 0.02–0.05° vs. 0.14–0.18° for the robot) and smaller springback distortions in truncated cones. Conversely, the robot achieved 45.6% lower surface roughness (e.g., 0.72–1.14 μm vs. 1.41–1.86 μm for CNC) across all geometries. Regarding forming forces, CNC exhibited 15–24% higher in-plane forces but 2–20% lower Z-forces compared to the robot, with total forces remaining similar (difference below 3%). Finite element simulations corroborated these trends but underestimated lateral forces due to shell-element limitations. These findings highlight the trade-offs between stiffness, accuracy, and surface quality, providing actionable insights for selecting SPIF systems based on application priorities.

Keywords SPIF · Stiffness · Forming forces · FEM · CNC · Roboforming

1 Introduction

The automotive, aerospace, and medical industries increasingly rely on components formed from metal sheets [1]. Traditional forming processes, such as stamping, are typically conducted at room temperature using mechanical presses and dies, offering high productivity for mass production [2]. However, these methods are less suitable for small batches or unique parts due to the high costs associated with tooling and setup. SPIF has emerged as a flexible and cost-effective alternative to address this limitation. SPIF employs a simple, inexpensive tool that follows a controlled path in at least three axes over a clamped blank sheet. The tool applies localized deformations along its trajectory, gradually shaping the material into its final form [3]. One of the key advantages of SPIF is the reduced forming forces due to the localized contact between the tool and the workpiece. This localized deformation also allows for higher limit strains compared to conventional stamping. However, SPIF has some drawbacks, including lower geometric precision, particularly in areas with small radii, and significant elastic recovery (springback) of the material [4]. Despite these challenges, the flexibility of SPIF enables its implementation on various platforms, such as ad hoc machines, milling machines [5], machining centers [4], and industrial robots [6]. This versatility has expanded the applications of SPIF, distinguishing it from conventional spinning processes by enabling the production of non-axisymmetric components [7].

✉ Antonio Sánchez Egea
antonio.egea@upc.edu

Alejandro Simoncelli
asimoncelli@inti.gob.ar

Luciano Buglioni
buglioni@inti.gob.ar

Daniel Martínez Krahmer
dmartinez@inti.gob.ar

1 Centro de Mecánica, Instituto Nacional de Tecnología Industrial, Av. General Paz 5445, Buenos Aires, Argentina

2 Departament d'Enginyeria Mecànica, Universitat Politécnica de Catalunya, Av. de Víctor Balaguer 1, Vilanova i la Geltrú 08800, Spain

Published online: 07 June 2025

The SPIF process has been widely studied for its ability to form lightweight alloys, such as aluminum, titanium, and stainless steel [8, 9]. Research has focused on optimizing process parameters, such as step size, wall angle, and tool rotation speed, to improve formability, geometric accuracy, and mechanical properties [10–12]. Lubrication has also been identified as a critical factor in reducing friction and material adhesion, particularly when forming softer materials like aluminum against harder tooling materials [13]. In addition to material considerations, the choice of equipment plays a significant role in SPIF. Industrial robots, for instance, offer increased flexibility and simplified setup configurations, enabling advanced techniques like dual-side incremental forming [14]. However, robots are generally more compliant than CNC machines, and their stiffness varies depending on joint configuration [15, 16]. This compliance can affect the precision and repeatability of the process, particularly under dynamic loading conditions. To address these challenges, models such as the virtual joint model have been developed to estimate end-effector stiffness and improve process control [17]. A critical aspect of SPIF research is the analysis of forming forces, which influence process limitations and equipment selection. These forces depend on material properties, sheet thickness, and process conditions [18]. Experimental studies have shown that step size, tool diameter, and forming angle significantly affect force distribution and material behavior [19]. A stepper forming angle and higher tensile strength coefficient generally result in higher forming forces, while increased tool rotation speeds can reduce these forces [20]. Geometric accuracy in SPIF is influenced by two primary factors: machine stiffness and material springback [21]. Machine stiffness, particularly in CNC machines and robots, directly impacts the precision of the formed parts. Finite element analysis has optimized machine structures, improving static stiffness and natural frequencies to achieve better surface finish and dimensional accuracy [22]. On the other hand, springback—the elastic recovery of the material after forming—remains a significant challenge. Numerical modeling has been employed to predict and mitigate springback, improving process design and part accuracy [23, 24].

This study combines experimental and numerical approaches to evaluate the influence of machine compliance in SPIF processes on geometric accuracy, forming forces, and springback behavior following sheet metal unclamping. The novelty of this work lies in its comprehensive investigation of the behavior of AISI 430 under SPIF, comparing the compliance of a milling machine and an industrial robot, both utilizing a free-rotating tool. We experimentally measure and model these effects using a finite element approach by addressing the displacements that occur when the formed blank is pre- and post-unclamping. This combined methodology provides valuable insights into the resulting springback and the post-fixture behavior of SPIF of parts, alongside an analysis of the forming forces influenced by machine stiffness. However, the main limitation of this study is the restricted range of joint configurations of the robot, which may not fully capture the potential of the behavior for larger or more complex geometries.

2 Methodology

2.1 Experimental assays

SPIF assays were conducted using a KUKA KR200-Comp 2 industrial robot and a CNC milling machine (Promecor 8 kW), as shown in Fig. 1. Three shapes, two truncate cones with constant wall angles of 35° and 55° and a complex concave-convex "shamrock" shape, were manufactured by SPIF under identical toolpath conditions to assess dimensional accuracy through 3D comparison (see Fig. 2). Toolpaths for these geometries were generated using AMPL Toolpaths [25] in a continuous anticlockwise downward spiral pattern, with a step of 0.25 mm for the truncated cones and 0.2 mm for shamrock, with a 4000 mm/min feed rate for all forming operations. The test material consisted of AISI 430 stainless steel sheets (see Table 1), each cut into 220 × 220 mm samples with a 0.577 ± 0.003 mm thickness, compliant with ASTM A240/EN 1.4016 standards. The forming tool featured a 15.1-mm diameter bearing ball, which rotated freely within a machined cavity at the end of an 18-mm steel

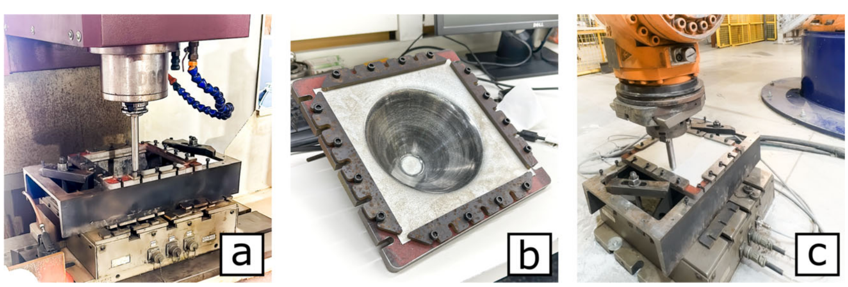

Fig. 1 **a** SPIF test on CNC. **b** Removable support. **c** SPIF test on the robot

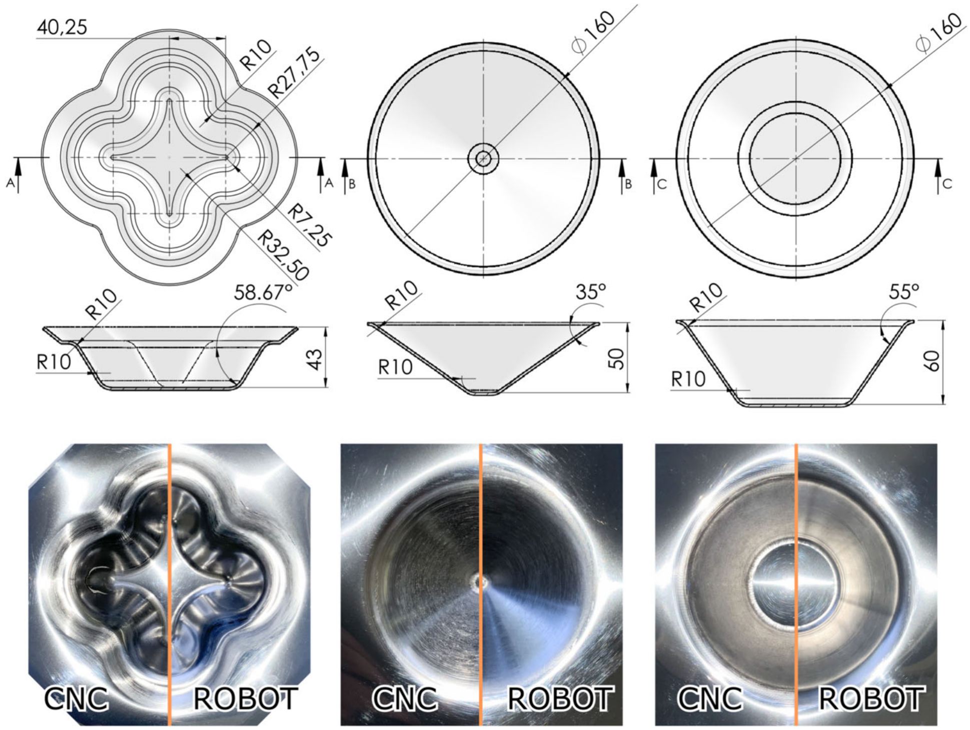

Fig. 2 Geometries of SPIF made shamrock shape and 35° and 55° truncated cones

bar and remained parallel to the z-axis on both machines during SPIF. Bearing grease (FETTE UP 20) was used as a lubricant on top of the sheet metal blank. The surface roughness parameter R_a was measured using a stylus profilometer (model: Taylor Hobson surtronic 3+) with a cut-off length (L_c) of 0.8 mm and a sampling length (L_n) of 4 mm. These parameters were selected to ensure accurate and consistent surface roughness measurements across the formed parts. Forces were recorded using a triaxial load cell and a Labjack T7 Pro DAQ with a sampling rate of 75 Hz. Once the forming process was completed, the formed parts were removed from the fixture while keeping the backplate of the frame clamped.

The 3D scanning was performed under both clamped and unclamped conditions using a structured-light HP 3D scanner (0.1 mm resolution) to accurately capture springback while minimizing measurement artifacts. For the clamped measurements, the fixture itself served as the alignment reference. For the unclamped condition, initial alignment was achieved via a three-point method by identifying three approximate corner points of the blank in the clamped state. This was followed by a local fine registration using a best-fit algorithm with rotations constrained about the Z-axis to prevent overfitting and to preserve relative springback between homologous points. Although this procedure minimizes global alignment error, it reduces the availability of depth references under the unclamped condition. Applying this strategy enabled the generation of global deviation maps for both clamped and unclamped states. A similar approach was then used to compare deviations among the CAD model, the physical part, and the FE simulation results. Subsequently, feature-specific dimensional analysis was conducted in Gom Inspect 2018: wall angles were measured by fitting a cone to intrinsic reference points on each mesh independently, ensuring those measurements remained unaffected by the pre- and post-unclamping or alignment steps.

Additionally, the local stiffness of each machine, robot, and CNC was determined by applying a load to the tool using a screw-driven linear actuator, maintaining the same orientation as during the SPIF, as shown in Table 2. The applied force was measured using a 3 kN load cell, while a Sylvac capacitive measuring probe, with a resolution of 0.1 μm, recorded the deflections. Multiple measurements were collected to generate linear regressions for evaluating the local stiffness at the work center position. Because the robot

Table 1 Chemical composition and mechanical properties of AISI 430 stainless steel [26]

Chemical composition (%)						Mechanical properties	
C	Si	Mn	P	S	Cr	$\sigma_{0.2\%}$ (MPa)	UTS (MPa)
<0.08	<1	<1	<0.04	<0.015	16–18	318	508

Table 2 Linear regression results for the stiffness of the CNC and robot

Machine	Direction	Stiffness (N/m)	Y-intercept (N)	R^2	Load range (N)
	X	1.370E+06	8.94	0.998	[0: 490]
CNC	*Y*	1.327E+06	21.90	0.996	[0: 470]
	Z	1.587E+07	4.39	0.999	[0: 784]
	X	3.969E+05	−8.50	0.998	[0: 490]
Robot	*Y*	2.690E+05	−10.40	0.996	[0: 490]
	Z	1.313E+06	2.50	0.999	[0: 784]

automatically engages its joint brakes when stationary, measurements were performed running 0.1 mm oscillations, so the joint breaks were disengaged and control loops remained active. Displacements were recorded perpendicular to the oscillation direction to minimize measurement errors. The modified Denavit-Hartenberg parameters and joint angles θ_{1-6}, as detailed in Table 3, define the kinematic configuration of the robot during these measurements and joint angle ranges reached during the process.

2.2 Numerical model

A dynamic FEM model with thermo-mechanical coupling was developed to simulate the SPIF process in *OpenRadioss*, an open-source solver. Shell elements represented the workpiece, supports and tools; the latter two were rigid. The model is divided into three steps: forming, supporting release, and dynamic relaxation. Regarding the last step, quasi-static simulation via a dynamic relaxation method is needed to minimize the dynamic effects for converging towards static equilibrium, the final shape achieved after springback. The dynamic effect is damped by introducing a diagonal damping matrix proportional to the mass matrix in the dynamic equation. A spring with 3 degrees of freedom was placed between the tools and a point following the toolpath to simulate the stiffness of the tool and machine system. A damping value of 100 Ns/m was included. The workpiece was assumed to be a four-node shell Q4 viscoelastic hourglass Belytschko [27] formulation with improved treatment of warped elements, also considering full geometric nonlinearities. This formulation has long been established in the forming industry due to its computational efficiency and robustness in handling large deformations typical of sheet metal processes. Its reduced integration approach, while less accurate for capturing localized effects like through-thickness shear, is particularly suited for thin-sheet applications where global deformation and forming forces are of primary interest. This formulation is a cornerstone in industrial simulations of stamping, incremental forming, and crashworthiness, offering a validated compromise between accuracy and performance [28]. Two integration points through the shell thickness were implemented. Contact between the workpiece and tool is modeled as a node-surface (master–slave) algorithm, assuming a heat exchange coefficient of 15 kW/(m^{2}K) and a frictionless behavior between the sample and tool. At the supports, no heat exchange is considered. Inelastic heat fractions (also known as the Taylor-Quinney coefficient) are set to 1.0. Thermal expansion is not considered. A plastic flow *Johnson-Cook* material model has been adopted for the sample:

$$\sigma = [A + B(\varepsilon_p)^n][1 + Cln(\dot{\varepsilon_p}/\dot{\varepsilon_0})][1 - ((T - T_0)/(T_m - T_0))^m] \tag{1}$$

Table 3 Modified Denavit-Hartenberg parameters and joint angles θ_{1-6} for the robot

Modified Denavit-Hartenberg parameters						
Parameter	Joint 1	Joint 2	Joint 3	Joint 4	Joint 5	Joint 6
α_i [°]	0	−90	0	−90	90	−90
a_i [mm]	0	350	1050	−45	0	0
θ_i [°]	0	0	−90	0	0	180
d_i [(mm]	750	0	0	1000	0	210
Joint angles range at center of the workpiece						
Range	Joint 1	Joint 2	Joint 3	Joint 4	Joint 5	Joint 6
Center [°]	−74.00	−22.17	87.37	0.00	24.79	−164.01
Max [°]	−71.18	−19.91	93.02	0.00	29.64	−161.36
Min [°]	−76.52	−23.79	80.47	0.00	20.18	−166.52
$\Delta\theta$ [°]	5.34	3.88	12.55	0.00	9.46	5.16

The material parameters are defined as A-359 MPa, B-327 MPa, C-0.0786, $\dot{\varepsilon_0}$-0.04, n-0.454, m-0.919, T_m-1425 $°C$ and T_0-20 $°C$ [29]. The initial temperature was set to 20 °C, and convection between the sample and ambient air at 20 °C was added. Time integration is explicit for this model. Considering this and the large overall process time, mass scaling was employed to reduce computation time by artificially increasing workpiece density. It was applied as a function of time, evaluated by the solver based on the maximum time step size and the *Courant* stability condition [30]. Simulations used advanced mass scaling with a 5.0E−5 s time step and a 1.5 mm element size, achieving a runtime of under 12 h on a Ryzen 9 5950X 16-core processor. Figure 3 shows results for three different meshes compared for a 2 mm, 1.5 mm, and 1 mm element size, respectively. The contact condition was the penalty method set as Radioss General Purpose Interface (TYPE7). Final simulations were conducted with spring stiffness reflecting the asymmetrical condition of the robot according to Table 2.

3 Results and discussion

This section presents the analysis of the geometrical accuracy, model accuracy, surface properties, and forming forces of the truncated cones and shamrock samples before and after unclamping, focusing on the effects of machine stiffness and material springback. The rigidity of the forming system is critical in ensuring dimensional accuracy, as machine compliance can introduce geometric deviations due to tool and workpiece deflections.

3.1 Dimensional accuracy and surface roughness

This section examines the geometric profiles of the cones and shamrock samples before and after unclamping, in contrast with the target CAD shape. The analysis reveals a notable stiffness difference between the two machines, particularly in their directional responses. In the XY plane, the robot demonstrates an asymmetric stiffness distribution, with a 32.2% variation at the specified joint configuration. The stiffness disparity between the robot and the CNC machine is further highlighted when comparing their directional stiffness values. The CNC machine is approximately 2.5, 4, and 11 times stiffer than the robot in the X, Y, and Z directions, respectively. Figure 4 shows the mentioned profiles, and Table 4 exhibits the results of the wall angle, fitted point standard deviation (using a surface-driven cone Gaussian fit), and Z-depth of the SPIF of the geometries formed using a CNC and a robot to reveal distinct trends in geometric accuracy before and after unclamping. The Z-depth values were calculated using the frame as the reference plane in the clamped condition. These results may be biased due to debris causing abrasive wear on the toolbar cavity, as well as initial zero errors and robot repeatability.

Considering regions not affected by peripheral bending (Z-depth below −12 mm), the CNC-formed parts adhere more closely to the target shape, exhibiting deviations of 2.24 ± 0.15 mm and 0.99 ± 0.17 mm for the constant wall angle geometries of 35° and 55°, respectively. In contrast, parts formed by the robot show larger deviations, with values of 2.34 ± 0.46 mm and 1.74 ± 0.70 mm. For the shamrock geometry, the maximum deviation is typically observed in the zone affected by bending [31], with values reaching −7.92 mm for the CNC, approximately 12% greater than observed for the robot, observable in lower-right graph in Fig. 4. Additionally, this geometry exhibited a mean deviation of 0.09 ± 1.86 mm in CNC, compared to 1.3 ± 2.12 mm for the robot; however, these values are not directly comparable due to a significant crack that developed during the CNC process.

Regarding wall angle accuracy, CNC-formed parts show angles closer to the CAD reference, with deviations of 0.02–

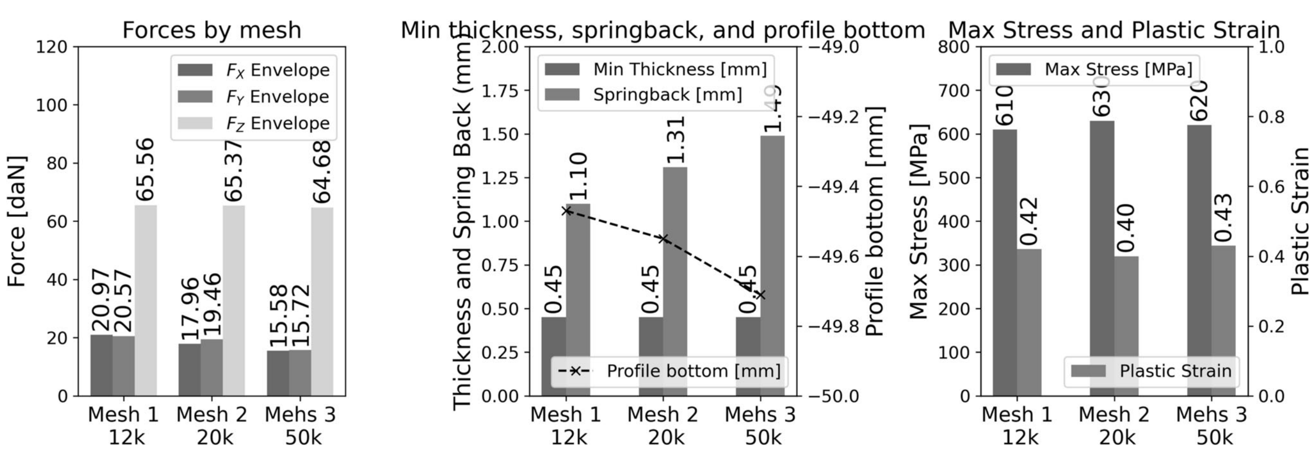

Fig. 3 Effect of mesh size on forces, thickness, springback, profile bottom, max stress, and plastic strain in 35^{a} truncate cone geometry

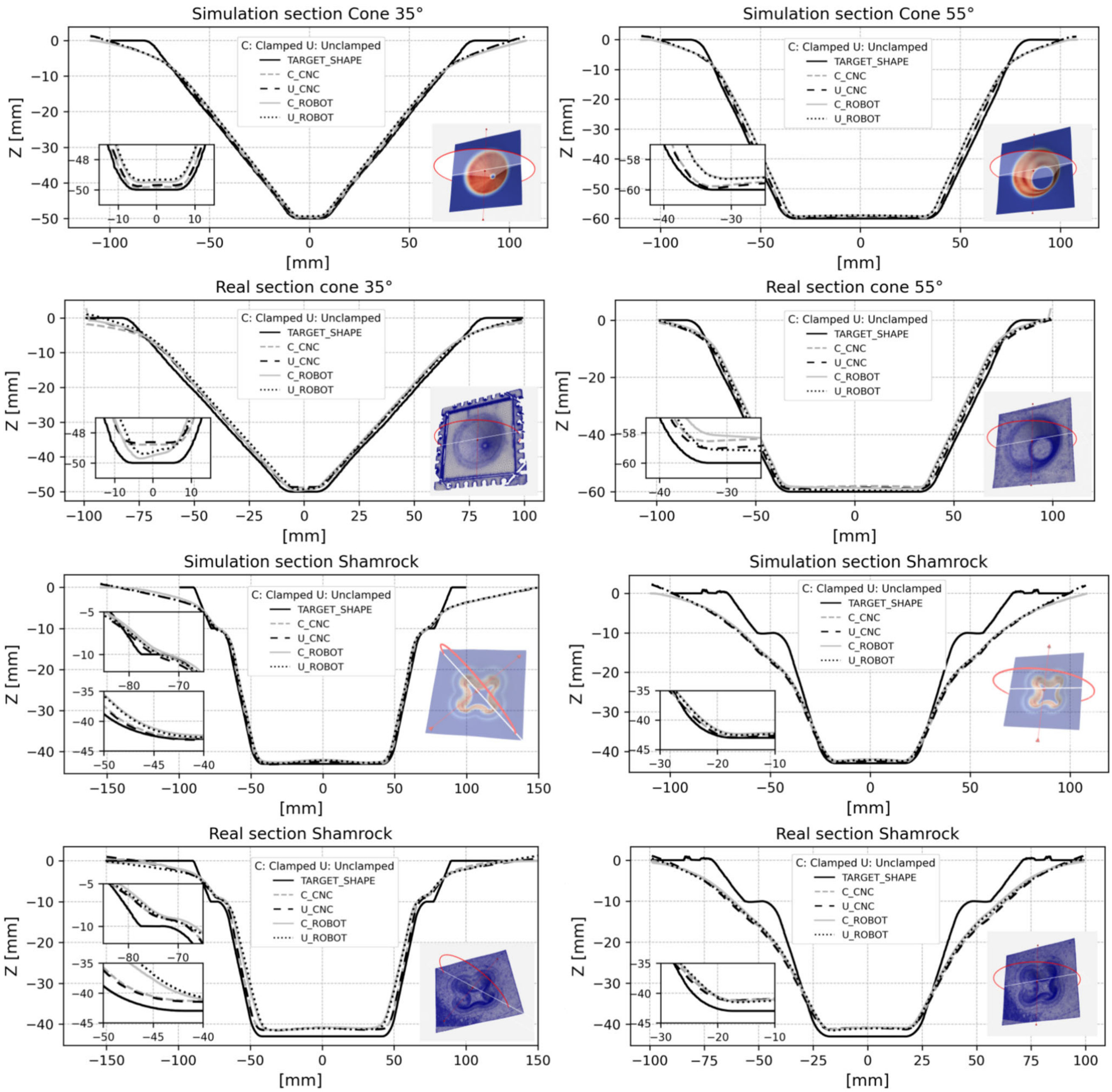

Fig. 4 Profiles of SPIF of the truncated cones, 35° and 55°, and shamrock shapes on CNC and robot, comparing target shapes with simulations and experimental results before and after unclamping

0.05° for 35° cones and 0.00–0.10° for 55° cones clamped and unclamped. Meanwhile, robot-formed parts exhibit greater discrepancies, reaching 0.14–0.18° for the clamped and unclamped conditions, respectively. For the shamrock geometry, the fitted wall angles were also closer to the target in CNC-formed parts, with deviations of 1.57° (concave - outer) and 12.5° (convex - inner) radius, compared to 3.36° (concave - outer) and 12.9° (convex - inner) radius for robot-formed parts. Similarly, the fitted point standard deviation is lower for CNC-formed parts than robot-formed parts, indicating better surface consistency and similar behavior in the *X* and *Y* directions. These results correspond to the final parts; the variation specifically induced by unclamping shows inconsistent trends, although greater deviations occur at the blank periphery. Comparisons with simulations indicate that CNC results align more closely with predictions, while roboforming SPIF exhibits noticeable discrepancies, particularly post-unclamping. These differences stem partly from model assumptions, such as using a shell approximation for the blank [32], which does not account for wear and

Table 4 Wall angles, fitted point, and Z-depth differences for CNC and robot in SPIF of geometries in clamped and unclamped conditions, including experimental and simulated values

Configuration	Fitted wall angle (°)	Fitted points SD (mm)	Z-depth (mm)
Cone 35° (FEM) - CNC Clamped	35.19	0.126	49.86
Cone 35° (FEM) - CNC Unclamped	35.21	0.096	49.77
Cone 35° (FEM) - Robot Clamped	35.09	0.226	49.59
Cone 35° (FEM) - Robot Unclamped	35.09	0.260	49.45
Cone 35° (Real) - CNC Clamped	35.02	0.065	48.09††
Cone 35° (Real) - CNC Unclamped	35.05	0.090	-†
Cone 35° (Real) - Robot Clamped	34.86	0.152	48.82††
Cone 35° (Real) - Robot Unclamped	34.82	0.147	-†
CAD - Cone 35°	**35**	-	**50**
Cone 55° (FEM) - CNC Clamped	55.16	0.322	59.84
Cone 55° (FEM) - CNC Unclamped	55.16	0.249	59.94
Cone 55° (FEM) - Robot Clamped	54.87	0.477	59.56
Cone 55° (FEM) - Robot Unclamped	54.87	0.416	59.56
Cone 55° (Real) - CNC Clamped	55.10	0.066	57.98††
Cone 55° (Real) - CNC Unclamped	55.00	0.172	-†
Cone 55° (Real) - Robot Clamped	54.94	0.151	59.08††
Cone 55° (Real) - Robot Unclamped	54.89	0.170	-†
CAD - Cone 55°	**55**	-	**60**
Shamrock (FEM) - CNC Clamped	58.25/48.46	0.159/0.134	42.44
Shamrock (FEM) - CNC Unclamped	58.30/48.53	0.153/0.133	42.57
Shamrock (FEM) - Robot Clamped	57.82/48.30	0.229/0.150	42.14
Shamrock (FEM) - Robot Unclamped	57.72/48.40	0.230/0.151	42.28
Shamrock (Real) - CNC Clamped	57.21/46.28	0.102/0.129	41.07††
Shamrock (Real) - CNC Unclamped	57.39/46.30	0.109/0.142	-†
Shamrock (Real) - Robot Clamped	55.59/46.06	0.118/0.152	40.40 ††
Shamrock (Real) - Robot Unclamped	55.42/45.88	0.149/0.164	-†
CAD - Shamrock (concave/convex)	**58.78/58.78**	-	**43**

† Accurate measurement was not possible due to the absence of a stable reference. †† Inclined fitted bottom planes and differences in the part origin between CNC and robot can lead to non-comparable results

The bold numbers represent the target geometry that was design by CAD

bending effects, and the assumption that the sheet metal is isotropic, overlooking potential material anisotropy.

The results reveal significant differences in springback behavior and geometric accuracy between CNC and robot-formed parts, driven by the stiffness disparity and directional responses of the two machines [16]. This effect is particularly notable in less constrained regions, such as blank edges. These deviations are attributed to both the lack of machine stiffness and residual stresses in the part at the end of the forming stage [33]. Also, alignment issues during 3D scanning further complicate the comparison between experimental geometries and FEM meshes or CAD references, as rotational discrepancies and springback effects hinder automatic alignment. To mitigate these deviations, alignment strategies can be improved by refining the blank edges and applying a "best-fit" alignment with z-rotation constraints. The best-fit algorithm minimizes the distance between the scanned model and the reference mesh, facilitating more accurate alignment [34].

Figure 5 illustrates the accuracy of the FEM model predicting real parts after unclamping. The deviation analysis for the 35° cone reveals moderate inward variations of approximately −0.68 mm for the robot and −0.36 mm for the CNC, alongside outward deviations of +0.69 mm and +0.75 mm, respectively. The geometrical deviation is pronounced between the two processes, as the wall angle is tilted or the geometry presents greater radii of curvature due to its geometrical complexity. The largest dispersions are found in the shamrock radii, reaching a maximum deviation of 2.62 mm in the robot compared to 1.61 mm in the CNC. These findings suggest that the lower stiffness and asymmetric response of the robot lead to greater geometric distortions, compared to

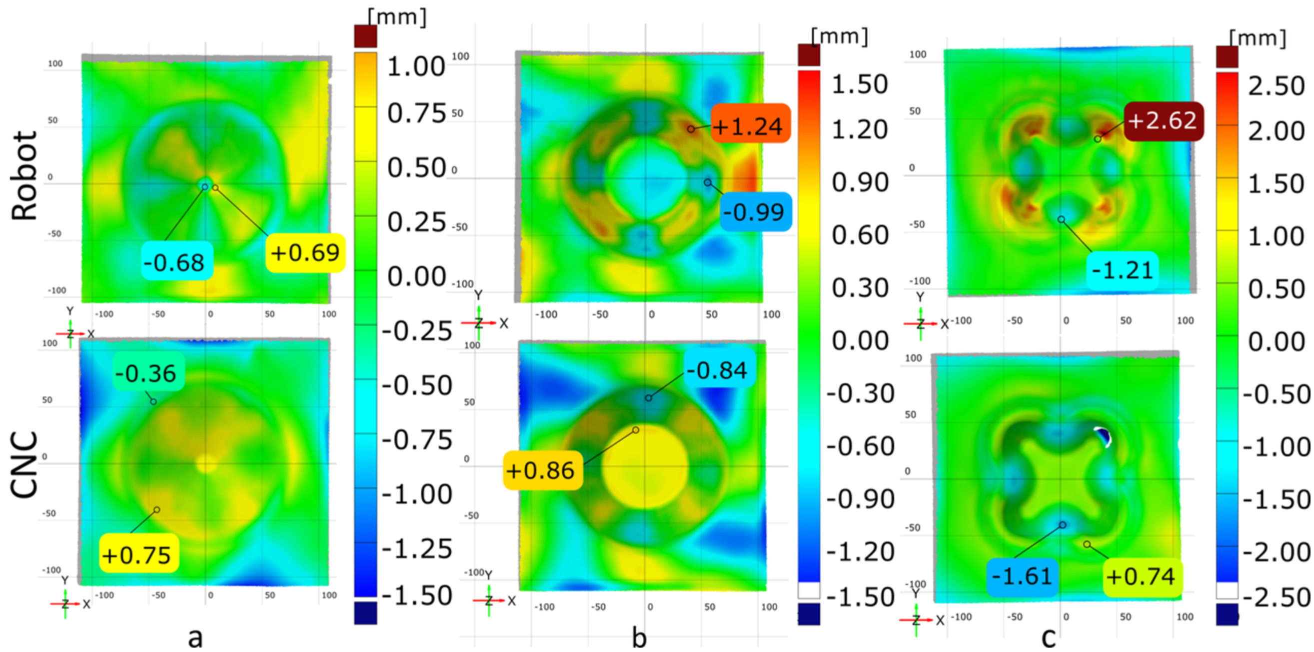

Fig. 5 Model accuracy in predicting unclamped SPIF of geometries, highlighting the minimum and maximum deviations: **a** 35° cone, **b** 55° cone, **c** shamrock

the more controlled deviations of the CNC. Additionally, the interaction between part geometry and machine compliance significantly influences springback behavior. Studies have shown springback-induced distortions are more pronounced in geometries with steeper wall angles. For example, research indicates that as the wall angle increases from 45 to 75°, the springback angle also increases, highlighting the geometry-dependent nature of springback [35]. Machine compliance, particularly in the robot, further affects springback outcomes. The inherent flexibility of robots can lead to deviations in the tool path during forming, resulting in increased elastic deformation and subsequent springback upon unloading. This compliance necessitates the development of compensation models to enhance the dimensional accuracy of formed parts [36]. These findings underscore the importance of optimizing toolpath strategies and incorporating machine-specific compliance effects into predictive models.

Regarding the surface properties, Table 5 exhibits the surface roughness in contact with the forming tool for all three geometries. As denoted in Fig. 2, the surface roughness seems to be affected differently depending on the forming process, showing worse surface quality for the machine with higher stiffness (CNC) than the one with higher compliance (robot). The results demonstrate a consistent 45.6% lower average roughness (Ra) in robot-formed parts (0.72–1.14 µm) compared to CNC-formed parts (1.41–1.86 µm). This significant difference stems from three interrelated factors related to machine compliance. First, the robot's lower stiffness allows passive vibration damping, evidenced by its 32–45% smaller force oscillations (Fig. 6). Second, its asymmetric XY stiffness distribution (32.2% variation) creates a self-regulating contact pressure that prevents localized stress peaks visible in CNC surfaces. Third, the robot's continuous servo adjustments maintain a more stable tool-workpiece interaction compared to the discrete interpolation of the CNC, despite both using G64 path smoothing. These observations align with Najm et al. [37], who attributed 48.7% of roughness variation to tool compliance effects. Our findings extend this understanding by demonstrating how system-level stiffness differences between CNC and robotic platforms propagate to surface finish, independent of identical tool geometries and lubrication conditions. The roughness advantage is most pronounced in steep wall angles (55° cone, 0.72 vs 1.62 µm), suggesting compliance becomes increasingly critical for maintaining surface quality under higher forming stresses.

Table 5 Surface roughness for the 35° and 55° truncated cones and shamrock geometries

Geometry†	Surface parameter	CNC (μm ± SD)	Robot (μm ± SD)
Cone 35°	R_a	1.41 ± 0.26	0.81 ± 0.04
Cone 55°	R_a	1.62 ± 0.26	0.72 ± 0.07
Shamrock	R_a	1.86 ± 0.5	1.14 ± 0.4

†The initial surface roughness of the sheet metal was 0.26 ± 0.01 µm

3.2 Forming forces

A comparative analysis of the forming forces in CNC and robot during the SPIF process reveals key differences in force distribution, magnitude, and variability between the two systems. Figure 6 shows the X and Y force components exhibit phase-shifted sinusoidal signals due to the spiral toolpath, a phenomenon well-documented in studies on SPIF toolpath strategies [38]. The forming forces measured during the process are summarized in Table 6, which presents the individual components (F_x, F_y, F_z) and the total force ($\overline{F_t}$) for both truncated cones and shamrock geometries that were manufactured by SPIF in the CNC or robot.

CNC in-plane forces show larger and more symmetric peak to peak amplitudes, typically around 67.3 daN for the 35° cone and 121.2 daN for the 55° cone. In contrast, robot in-plane forces in the X and Y directions display differing amplitudes, approximately 54.0 and 98.6 daN for the 35° and 55° truncated cones, respectively, reflecting the asymmetric stiffness of the robot. Despite the lower rigidity of the robot, z-direction forces exceed those in the CNC process, reaching up to 96.7 daN for the 55° cone, compared to 94.5 daN in the CNC case. The $\overline{F_t}$ remains comparable, with values of 86.6 daN (CNC) vs. 86.9 daN (robot) for the 35° cone and 104.9 daN (CNC) vs. 105.6 daN (robot) for the 55° cone, suggesting that both systems operating under similar conditions using the same tool achieve sufficient force to overcome flow stress and induce material deformation but through distinct force distribution strategies, as highlighted in similar research [15].

The complex shamrock geometry exhibits a distinctive force graph characterized by two primary regions. In the first region, a constant wall angle is maintained, exhibiting behavior similar to previous cases and culminating in a flat area where the load values drop to nearly zero. The force

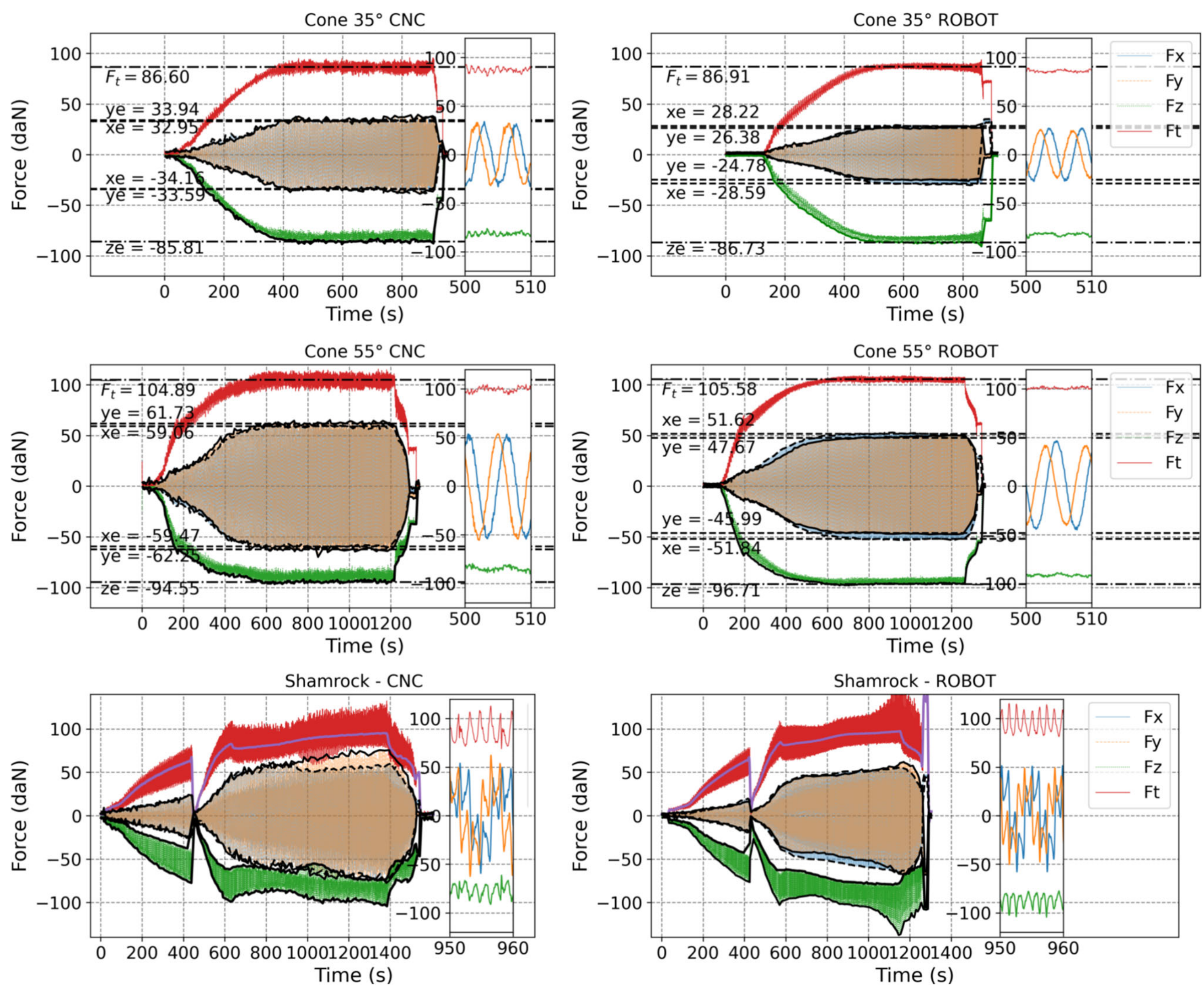

Fig. 6 Forming forces (F_x, F_y, F_z) and total ($\overline{F_t}$) for truncated cones and shamrock shapes, highlighting the mean saturation envelope and signal waveform

Table 6 Forming forces for truncated cones and shamrock geometries

Geometry	Force component	CNC (daN ± SD)	Robot (daN ± SD)	$\triangle F^{\dagger}$ (%)
Cone 35°	Peak to peak F_x	67.10 ± 1.87	56.81 ± 0.74	−15.3
	Peak to peak F_y	67.52 ± 1.95	51.15 ± 0.66	−24.2
	F_z	−85.81 ± 0.98	−86.73 ± 0.53	+1.1
	$\overline{F_t}$	86.61 ± 2.74	86.91 ± 1.29	+0.3
Cone 55°	Peak to peak F_x	118.52 ± 1.67	103.46 ± 1.05	−12.7
	Peak to peak F_y	123.98 ± 2.41	93.66 ± 0.95	−24.5
	F_z	−94.55 ± 0.97	−96.71 ± 0.54	+2.3
	$\overline{F_t}$	104.89 ± 3.62	105.58 ± 1.23	+0.7
Shamrock††	Peak to peak F_x	126.2 ± 5.0†††	118.0 ± 0.8	−6.5
	Peak to peak F_y	145.4 ± 4.2†††	120.8 ± 1.2	−16.9
	F_z	−101.81 ± 0.89†††	−130.2 ± 4.19	+27.9
	$\overline{F_t}$	95.26 ± 12.9	96.82 ± 13.25	+1.6

†Average force variation for the two forming processes. ††The forming forces correspond to 20 s before the peak forming force. †††A fracture on CNC Shamrock occurred before this point

shows a waveform in the second region, with peak values in the concave, near to frame sections and minima in the convex sections, consistent with findings reviewed on complex geometries in SPIF [38]. Both setups exhibit similar force trends, increasing total forces as the process progresses, up to approximately 95 daN average for the CNC system and 97 daN average for the robot. The CNC system shows larger oscillations in all force components and total force, indicating higher dynamic interactions between the tool and the sheet. In contrast, the robot demonstrates smoother force profiles with lower amplitude fluctuations, suggesting that its smoother path and inherent compliance may help absorb vibrations, leading to more stable force patterns [15]. These results imply that while CNC SPIF benefits from higher rigidity, it may require vibration damping strategies to improve process stability. Nevertheless, roboforming SPIF could leverage its flexibility for enhanced surface quality and reduced tool wear.

FEM simulations showed good prediction of the vertical force component F_z. For the CNC platform, forces of −79.26 daN and −100.4 daN were obtained for the 35° and 55° cone geometries, respectively, corresponding to deviations of −7.6% and 6.2% compared to experimental values. On the robot, values of −81.31 daN and −101.08 daN were observed in the stable deformation zone, with deviations of −6.2% and 4.2%, respectively. Regarding the in-plane forces (F_x, F_y), the waveforms appear distorted, losing their sinusoidal shape and approximating a sawtooth profile. This distortion can partly be attributed to the orthogonal mesh used in the FEM model, as well as the Rayleigh damping implemented, both of which influence the dynamic behavior of the process. Additionally, transient effects were observed at the beginning of each spiral loop, caused by instantaneous variations in toolpath velocity. These transients are generally more evident in the CNC simulation due to its higher stiffness and they hinder direct comparison of the force envelopes. To overcome this, $\sqrt{2}$ RMS values were computed as an approximation of the expected amplitude of a sinusoidal signal. Furthermore, the magnitude of the resultant planar force $F_p = (F_x^2 + F_y^2)^{1/2}$ was calculated, as shown in Figs. 7 and 8. This metric shows underestimated results relative to the experimental data. For the CNC system, deviations of −38.2%, −26.9% and −17.8% were observed for the 35° and 55° cones and the shamrock, respectively; for the robot, deviations of −26.9%, −21.6%, and −13.4% were obtained. This behavior may indicate improved predictive accuracy for the lower stiffness system, which could be related to the smaller fictitious mass introduced by advanced mass scaling to maintain an identical time step in both simulations.

4 Conclusion

This work examines the significant stiffness differences between CNC and robot in SPIF and their effects on geometric accuracy, surface roughness, and forming forces. The key conclusions are as follows:

- CNC-formed parts show superior wall angle accuracy with smaller deviations (0.02–0.05°) compared to the robot (0.14–0.18°). The formation of debris during the process contributes to premature tool wear and leads to significant discrepancies in Z-depth. Also, the robot outperformed CNC in reducing 45% of the surface rough-

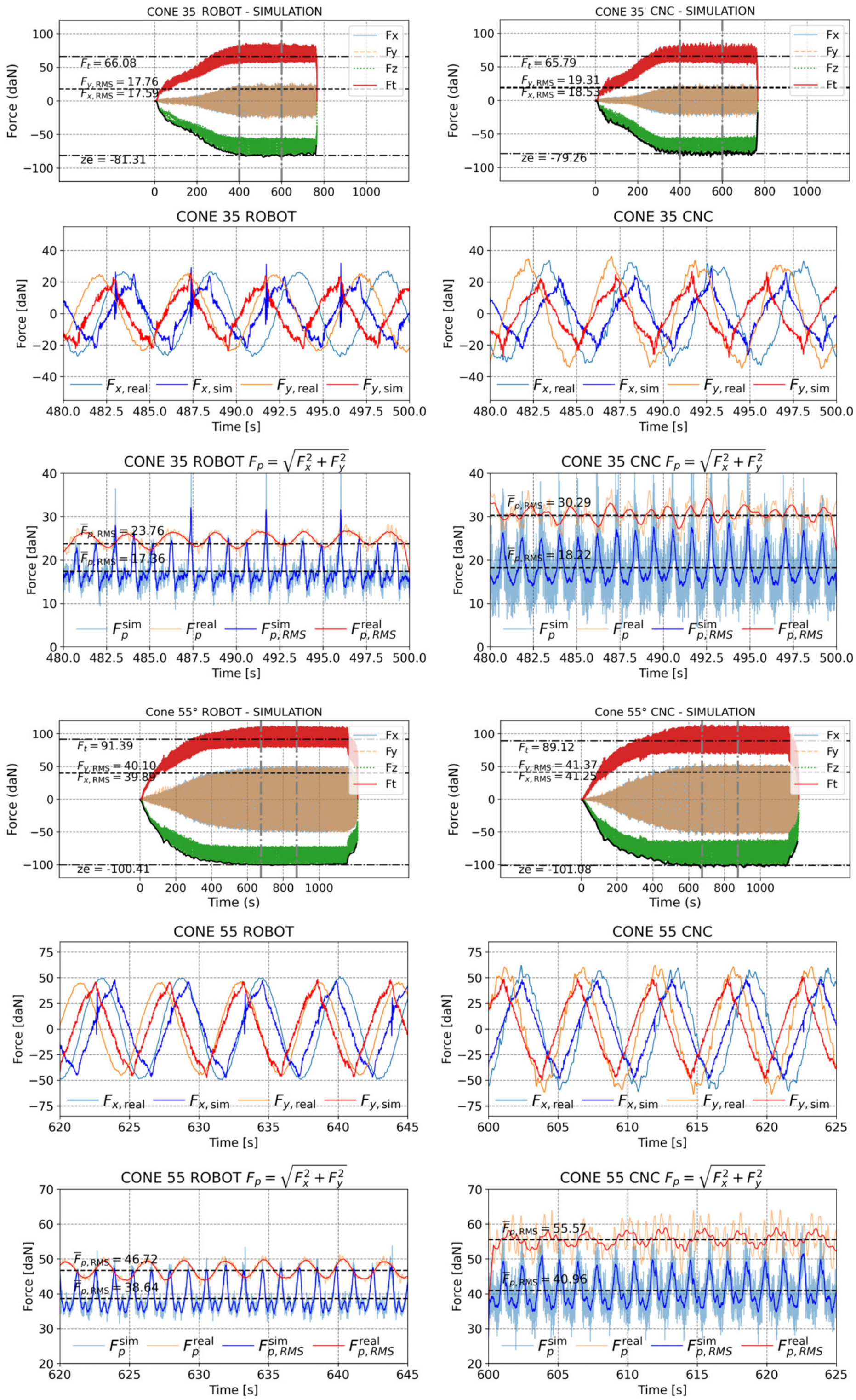

Fig. 7 FEM forces (F_x, F_y, F_z) and total force ($\overline{F_t}$) for 35° and 55° cone. The calculation region and the values of $\sqrt{2}F_{\mathrm{RMS}}$ are highlighted. A detailed view shows the RMS values computed over one-eighth of the signal period for the experimental data and with a fixed 0.125 s window for the simulations, as well as the in plane magnitudes F_p and $\overline{F_p}$

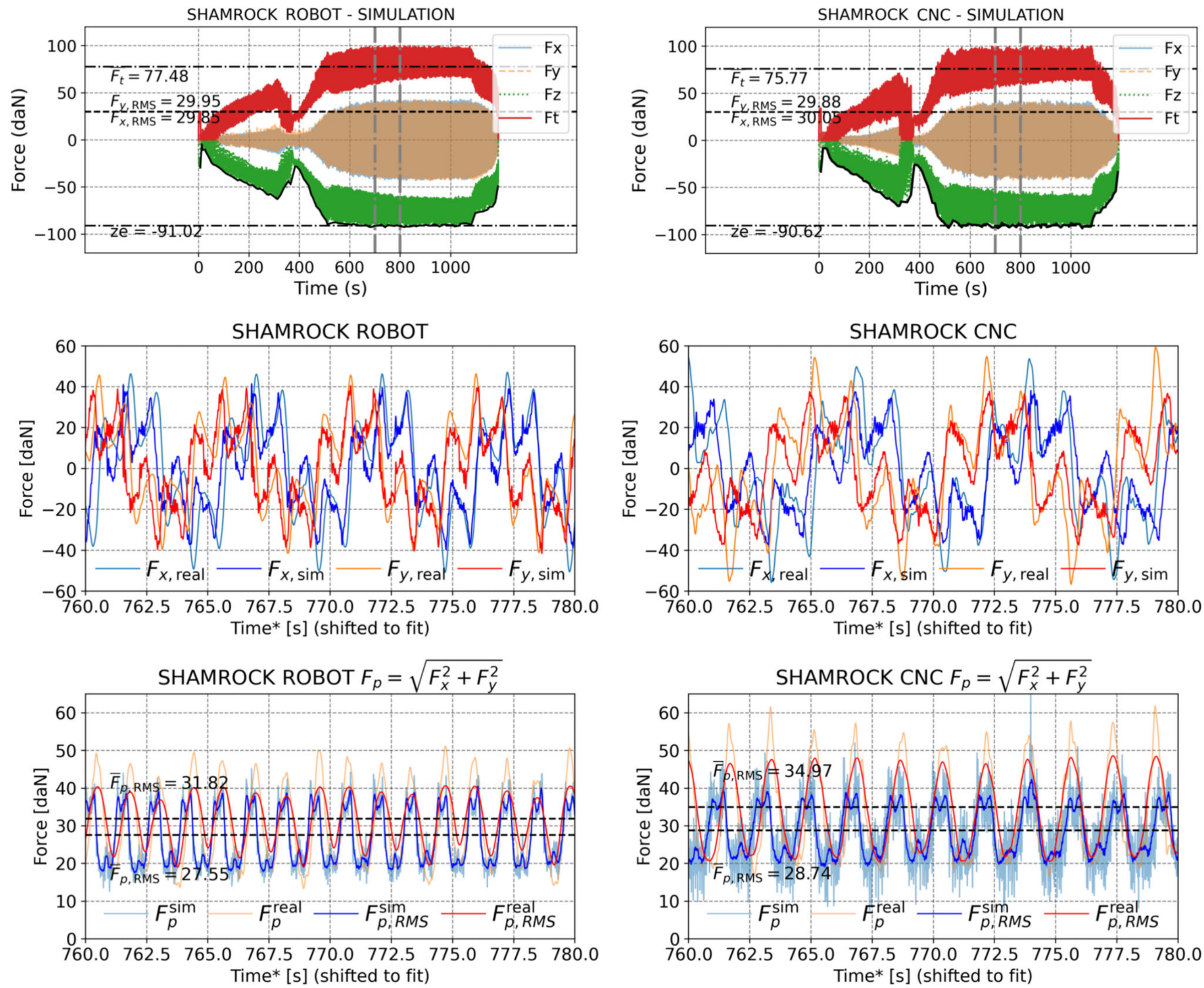

Fig. 8 FEM forces (F_x, F_y, F_z) and total force ($\overline{F_t}$) for the shamrock. The calculation region and the values of $\sqrt{2}F_{\mathrm{RMS}}$ are highlighted. A detailed view shows the RMS values computed over one-eighth of the signal period for the experimental data and with a fixed 0.125 s window for the simulations, as well as the magnitudes in plane F_p and $\overline{F_p}$

ness, likely due to its smoother toolpath and greater compliance in reducing tool-surface interactions.

- CNC required around 10–20% higher in-plane forces and 2–20% lower z-forces depending on the geometry to SPIF. Moreover, CNC produced more oscillatory forces, indicating stronger dynamic interactions, while the robot exhibited smoother force profiles with lower fluctuations, further supporting its ability to absorb vibrations.
- Simulations confirmed higher geometric accuracy in the CNC platform, with vertical force errors of -7.6% and 6.2% for 35° and 55° cones, respectively. However, lateral forces were underestimated, with mean planar force $\overline{Fp}$ RMS deviations of -38.2%, -26.9%, and -17.8%, for the 35°, 55°, and shamrock geometries, respectively. The robotic setup showed vertical force deviations of up to 6.2%, but achieved better lateral force prediction, with $\overline{Fp}$ RMS deviations of -26.9%, -21.6%, and -13.4%. The robot's lower stiffness also resulted in faster accumulation of spring energy, indicating higher sensitivity to deformation under identical time step conditions.

Further research should refine pre- and post-unclamping analysis using 3D scans to quantify alignment variations and their impact on geometric accuracy. Also, while total forming forces were similar to the experimental, the asymmetric stiffness and deformation behavior of the robot require further investigation to optimize process control and predictive modeling.

Acknowledgements We acknowledge the support of the Serra Húnter program (Generalitat de Catalunya) and the Fondo de Innovación Tecnológica de Buenos Aires (FITBA). Our sincere thanks also go to Rafael Dahl and Cristian Raspanti for allowing us to use the robot for research and testing.

Author contribution Alejandro Simoncelli: investigation, methodology, visualization. Luciano Buglioni: numerical simulation, formal analysis, visualization. Daniel Martínez Krahmer: literature review, methodology, writing—original draft. Antonio J. Sánchez Egea: supervision, writing—original draft, writing—review and editing.

Funding This work was supported by the Serra Húnter program (Generalitat de Catalunya) under reference number UPC-LE-304 (2018) and the Fondo de Innovación Tecnológica de Buenos Aires (FITBA) under reference number 2024-319A.

Declarations

Conflict of interest The authors declare no competing interests.

References

1. Altan T, Tekkaya AE (2012) Sheet metal forming: processes and applications. https://doi.org/10.31399/asm.tb.smfpa.9781627083171
2. Boljanovic V (2004) Sheet metal forming processes and die design
3. Nallagundla VR, Lingam R, Cao J (2015) In: Nee AYC (ed) Incremental metal forming processes in manufacturing, Springer, London, pp 411–452. https://doi.org/10.1007/978-1-4471-4670-4_45
4. Ajay M, Kant R (2020) Incremental sheet forming technologies: principles, merits, limitations, and applications (1st ed).https://doi.org/10.1201/9780429298905
5. Resende TP, Carmo GP, Afonso DG, Sousa RJ (2024) Development of a compact incremental forming machine. Mach 12(2). https://doi.org/10.3390/machines12020086
6. Ostasevicius V, Paulauskaite-Taraseviciene A, Paleviciute I, Jurenas V, Griskevicius P, Eidukynas D, Kizauskiene L (2022) Investigation of the robotized incremental metal-sheet forming process with ultrasonic excitation. Mater 15(3). https://doi.org/10.3390/ma15031024
7. Wang L, Long H (2011) Investigation of material deformation in multi-pass conventional metal spinning. Mater Des 32(5):2891–2899. https://doi.org/10.1016/j.matdes.2010.12.021
8. Ortiz M, Penalva M, Iriondo E, Arroyo B, Pereira O, Rodríguez A (2020) Investigation of thermal-related effects in hot SPIF of Ti–6Al–4V alloy. Int J Precis Eng Manuf-Green Technol 7:299–317. https://doi.org/10.1007/s40684-019-00038-z
9. Kumar R, Kumar V, Kumar A (2023). A review on effect of computer-aided machining parameters in incremental sheet forming. https://doi.org/10.1002/9781119986454.ch3. Chap. 3
10. Żaba K, Puchlerska S, Kuczek Ł, Trzepieciński T, Maj P (2022) Effect of step size on the formability of Al/Cu bimetallic sheets in single point incremental sheet forming. Materials 16(1):367. https://doi.org/10.3390/ma16010367
11. Zhang Y, Zhang Z, Li Y, Hu L, Pang Q, Hu Z (2023) Investigation of pre-aged hardening single-point incremental forming process and mechanical properties of AA6061 aluminum alloy. Mater 16(11):4154. https://doi.org/10.3390/ma16114154
12. Tang Z, Xiong W, Zheng Y, Zhang J (2023) The effects of forming angle on the geometry accuracy and mechanical properties of Al-Li alloy truncated pyramids by single point incremental forming. Appl Sci 13(10):6144. https://doi.org/10.3390/app13106144
13. Trzepiecinski T, Oleksik V, Pepelnjak T, Najm S, Paniti I, Maji K (2021) Emerging trends in single point incremental sheet forming of lightweight metals. Metals - Open Access Metall J 11:1188. https://doi.org/10.3390/met11081188
14. Valoppi B, Sánchez Egea AJ, Zhang Z, González Rojas HA, Ghiotti A, Bruschi S, Cao J (2016) A hybrid mixed double-sided incremental forming method for forming Ti6Al4V alloy. CIRP Ann 65(1):309–312. https://doi.org/10.1016/j.cirp.2016.04.135
15. Meier H, Laurischkat R, Zhu J (2011) A model based approach to increase the part accuracy in robot based incremental sheet metal forming. AIP Conf Proc 1:1407–1412. https://doi.org/10.1063/1.3552383
16. Bharti S, Paul E, Uthaman A, Krishnaswamy H, Klimchik A, Abraham Boby R (2024) Systematic analysis of geometric inaccuracy and its contributing factors in roboforming. Sci Rep 14(1):20291
17. Paul E, Bharti S, Uthama A, Boby RA, Krishnaswamy H, Klimchik A (2023) Evaluation of deviations due to robot configuration for robot-based incremental sheet metal forming. In: Proceedings of the 2023 6th International Conference on Advances in Robotics. AIR '23. Association for Computing Machinery, New York, NY, USA. https://doi.org/10.1145/3610419.3610471
18. Bârsan A, Crenganiş M, Popp MO, Rusu GP (2020) Roboforming - investigations regarding forming forces in SPIF process. Acta Univ Cibiniensis Tech Ser 72(1):37–41. https://doi.org/10.2478/aucts-2020-0006
19. Kilani L, Mabrouki T, Ayadi M, Chermiti H, Belhadi S (2020) Effects of rolling ball tool parameters on roughness, sheet thinning, and forming force generated during SPIF process. Int J Adv Manuf Technol 106(9/10):4123. https://doi.org/10.1007/s00170-019-04918-1
20. Torsakul S, Kuptasthien N (2019) Effects of three parameters on forming force of the single point incremental forming process. J Mech Sci Technol 33(6). https://doi.org/10.1007/s12206-019-0528-2
21. Wei H, Zhou L, Heidarshenas B, Ashraf IK, Han C (2019) Investigation on the influence of springback on precision of symmetric-cone-like parts in sheet metal incremental forming process. Int J Light Mater Manuf 2(2):140–145. https://doi.org/10.1016/j.ijlmm.2019.05.002 . Advances in forming and joining of lightweight structures
22. Chan TC, Ullah A, Roy B, Chang SL (2023) Finite element analysis and structure optimization of a gantry-type high-precision machine tool. Sci Rep 13(1):13006. https://doi.org/10.1038/s41598-023-40214-5
23. Firat M, Kaftanoglu B, Eser O (2008) Sheet metal forming analyses with an emphasis on the springback deformation. J Mater Process Technol 196(1):135–148. https://doi.org/10.1016/j.jmatprotec.2007.05.029
24. Hetz P, Merklei M (2024) Numerical springback prediction for high-strength aluminum alloys based on the sheet metal upset-

ting test. Proc IME B J Eng Manufact. https://doi.org/10.1177/09544054241289996
25. Malhotra R, Reddy NV, Cao J (2010) Automatic 3D spiral toolpath generation for single point incremental forming. J Manuf Sci Eng 132(6). https://doi.org/10.1115/1.4002544
26. Milutinovic M, Lendjel R, Balos S, Zlatanovic D, Sevsek L, Pepelnjak T (2021) Characterisation of geometrical and physical properties of a stainless steel denture framework manufactured by single-point incremental forming. J Mater Res Technol 10:605–623. https://doi.org/10.1016/j.jmrt.2020.12.014
27. Belytschko T, Leviathan I (1992) Physical stabilization of the 4-node shell element with one-point quadrature. Comput Methods Appl Mech Eng 113:321–350. https://doi.org/10.1016/0045-7825(94)90052-3
28. Rosca N, Oleksik M, Rosca L (2021) Numerical-experimental study regarding the single point incremental forming process. MATEC Web Conf 343:03008. https://doi.org/10.1051/matecconf/202134303008
29. Korkmaz ME (2020) Verification of Johnson-Cook parameters of ferritic stainless steel by drilling process: experimental and finite element simulations. J Mater Res Technol 9(3):6322–6330. https://doi.org/10.1016/j.jmrt.2020.03.045
30. Engineering A (2017) Introduction to explicit analysis using RADIOSS. Altair Engineering, Inc., Troy, Michigan, USA. Technical documentation for RADIOSS, a finite element analysis solver for explicit dynamics. https://www.altair.com/
31. Centeno G, Bagudanch I, Garcia-Romeu ML, Martinez-Donaire AJ, Vallellano C (2016) Experimental study on the overall spifability of AISI 304 sheets under different bending conditions. Key Eng Mater 554–557:2293–2298. https://doi.org/10.4028/www.scientific.net/KEM.554-557.2293. Online 13 June 2013
32. Moser N (2019) Deformation mechanisms and process planning in double-sided incremental forming. PhD thesis, Northwestern University (December 2019)
33. Giraud-Moreau L, Belchior J, Lafon P, Lotoing L, Cherouat A, Courtielle E, Guines D, Maurine P (2018) Springback effects during single point incremental forming: optimization of the tool path. AIP Conf Proc 1960. https://doi.org/10.1063/1.5035035
34. Abdelmajid Y (2012) Investigation and comparison of 3D laser scanning software packages. Master of science thesis, Royal Institute of Technology (KTH), Stockholm, Sweden
35. Mezher MT, Barrak OS, Nama SA, Shakir RA (2021) Predication of forming limit diagram and spring-back during SPIF process of AA1050 and DC04 sheet metals. J Mech Eng Res Dev 44(1):337–345
36. Shaker W, Klimchik A (2024) Robot-based incremental forming: springback effect compensation model for various materials. In: 2024 10th international conference on control, decision and information technologies (CoDIT). https://doi.org/10.1109/CoDIT62066.2024.10708300
37. Najm SM, Paniti I (2021) Predict the effects of forming tool characteristics on surface roughness of aluminum foil components formed by SPIF using ANN and SVR. Int J Precis Eng Manuf 22:13–26. https://doi.org/10.1007/s12541-020-00434-5
38. Duflou JR, Habraken AM, Cao J et al (2018) Single point incremental forming: state-of-the-art and prospects. Int J Mater Form 11:743–773. https://doi.org/10.1007/s12289-017-1387-y